

See discussions, stats, and author profiles for this publication at: <https://www.researchgate.net/publication/51100741>

# Influence of the 316 L Stainless Steel Interface on the Stability and Barrier Properties of Plasma Fluorocarbon Films

ARTICLE in ACS APPLIED MATERIALS & INTERFACES · JUNE 2011

Impact Factor: 6.72 · DOI: 10.1021/am200245d · Source: PubMed

CITATIONS

7

READS

45

7 AUTHORS, INCLUDING:



François Lewis

Teledyne DALSA

12 PUBLICATIONS 111 CITATIONS

SEE PROFILE



Pascale Chevallier

Laval University

65 PUBLICATIONS 594 CITATIONS

SEE PROFILE



J.-J. Pireaux

University of Namur

406 PUBLICATIONS 7,570 CITATIONS

SEE PROFILE



Diego Mantovani

Laval University

189 PUBLICATIONS 2,814 CITATIONS

SEE PROFILE

# Influence of the 316 L Stainless Steel Interface on the Stability and Barrier Properties of Plasma Fluorocarbon Films

François Lewis,<sup>†,‡</sup> Maxime Cloutier,<sup>†</sup> Pascale Chevallier,<sup>†</sup> Stéphane Turgeon,<sup>†</sup> Jean-Jacques Pireaux,<sup>§</sup> Michael Tatoulian,<sup>‡</sup> and Diego Mantovani<sup>\*,†</sup>

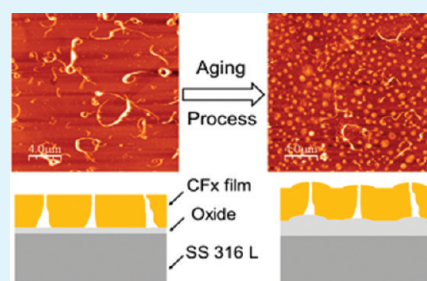
<sup>†</sup>Laboratory for Biomaterials and Bioengineering, Department of Materials Engineering & University Hospital Research Center, Laval University, Quebec City, QC, G1K 7P4, Canada

<sup>‡</sup>Laboratoire de Génie des Procédés Plasmas et Traitement de Surfaces, Université Pierre et Marie Curie, ENSCP, 11 rue Pierre et Marie Curie, 75005 Paris, France

<sup>§</sup>Laboratoire Interdisciplinaire de Spectroscopie Electronique, FUNDP - University of Namur, 61 Rue de Bruxelles, B-5000 Namur, Belgium

**ABSTRACT:** Coatings are known to be one of the more suited strategies to tailor the interface between medical devices and the surrounding cells and tissues once implanted. The development of coatings and the optimization of their adhesion and stability are of major importance. In this work, the influence of plasma etching of the substrate on a plasma fluorocarbon ultrathin coating has been investigated with the aim of improving the stability and the corrosion properties of coated medical devices. The 316 L stainless steel interface was subjected to two different etching sequences prior to the plasma deposition. These plasma etchings, with H<sub>2</sub> and C<sub>2</sub>F<sub>6</sub> as gas precursors, modified the chemical composition and the thickness of the oxide layer and influenced the subsequent polymerization. The coating properties were evaluated using flat substrates submitted to deformation, aging into aqueous medium and corrosion tests. X-ray photoelectron spectroscopy (XPS), time of flight-secondary ion mass spectrometry (ToF-SIMS), ellipsometry, and atomic force microscopy (AFM) were performed to determine the effects of the deformation and the aging on the chemistry and morphology of the coated samples. Analyses showed that plasma etchings were essential to promote reproducible polymerization and film growth. However, the oxide layer thinning due to the etching lowered the corrosion resistance of the substrate and affected the stability of the interface. Still, the deformed samples did not exhibit adhesion and cohesion failure before and after the aging.

**KEYWORDS:** interface, stability, corrosion, plasma treatments, fluoropolymers, etching



## 1. INTRODUCTION

Plasma polymerization has been developed in various fields during the last decades, particularly for optical, electronical, and biomedical applications. The coating chemistry and properties can be tailored according to the needs and the plasma polymerization of a wide variety of precursors such as methacrylate,<sup>1</sup> pyridine,<sup>2</sup> allylamine,<sup>3,4</sup> hydrocarbon,<sup>5</sup> organosilicone,<sup>6,7</sup> and fluorocarbon<sup>8–10</sup> monomers, has been reported. Indeed, depending on the precursors and the plasma parameters, the coating could exhibit different properties and functionalities. When compared with other thin film deposition techniques, plasma-deposited coatings generally displayed a higher interfacial adhesion, as well as a better chemical stability over time.<sup>11–15</sup> Moreover, plasma treatments provide the possibility to tailor the surface properties with functionalization and film deposition without affecting the bulk mechanical properties.<sup>12,16</sup> This unique combination of characteristics makes plasma polymerization an ideal option for the deposition of an effective and stable barrier coating for biomedical devices, where enhanced surface biocompatibility is required. It should be noted that the term barrier is used to describe the coating ability to protect the device from corrosion, as previously reported by Bierwagen et al.<sup>17</sup>

Plasma polymerization techniques are particularly interesting for the coating of stents, which are thin wire mesh tubes, mainly made of 316 L stainless steel (SS316L), used to provide an internal scaffolding to diseased arteries and to prevent the obstruction of blood flow.<sup>18</sup> Despite displaying excellent bulk mechanical properties essential for biomedical applications, stainless steel is naturally covered with a layer composed of chromium and iron oxides, which is brittle and mechanically unstable under stress.<sup>19</sup> Moreover, the oxide layer can also be degraded in the contact of body fluids, and then permits the release of potentially toxic ions, limiting its biocompatibility.<sup>19,20</sup> One solution is the development of coated and/or drug-eluting stents<sup>21</sup> which could prevent the release of carcinogenic ions<sup>19,22</sup> and/or the reclosure of the diseased artery (restenosis). However, in-stent restenosis, thrombosis, stent fractures, and coating failures are still prevalent.<sup>23–30</sup> The coating failure in current commercialized coated stents could be explained by the poor film–substrate adhesion as they are coated by spraying or dipping.<sup>30,31</sup> As plasma polymerization is known to promote

**Received:** February 27, 2011

**Accepted:** May 5, 2011

**Published:** May 05, 2011

Table 1. Plasma treatment parameters

params	etchings		polymerization
	C <sub>2</sub> F <sub>6</sub>	H <sub>2</sub>	C <sub>2</sub> F <sub>6</sub> + H <sub>2</sub>
peak power (W)	100	100	150
duty cycle	25% ( $t_{\text{on}} = 100$ ms; $t_{\text{off}} = 300$ ms)	25% ( $t_{\text{on}} = 100$ ms; $t_{\text{off}} = 300$ ms)	5.3% ( $t_{\text{on}} = 5$ ms; $t_{\text{off}} = 90$ ms)
gas pressure (mbar)	0.200	0.930	0.930
gas flow rate (sccm)	5	10	19.0 for C <sub>2</sub> F <sub>6</sub> and 1.2 for H <sub>2</sub>
distance to the powered antenna (cm)	6	6	11
treatment time (s)	100	100	300

film adhesion, this technique has been used in this work. Moreover, since expanded polytetrafluoroethylene (ePTFE) has already been successfully used in a number of biomedical applications,<sup>32–37</sup> fluorocarbon films (CF<sub>x</sub>) were selected for this specific application.

In this context, CF<sub>x</sub> plasma deposition on SS316L has been investigated and previous results showed promising adhesion properties for the fluorocarbon films after a plastic deformation similar to a stent expansion.<sup>38–40</sup> Previous characterizations by near-edge X-ray absorption fine structure (NEXAFS)<sup>41</sup> showed the occurrence of nanodefects, which led to water diffusion during immersion in aqueous medium and resulted in chemical modifications and reorganization of the coating.<sup>42</sup> To lower the nanodefects density, to promote the film growth and to increase the film stability, we applied different plasma etching sequences prior to the coating deposition. C<sub>2</sub>F<sub>6</sub><sup>43,44</sup> and H<sub>2</sub><sup>45–48</sup> precursors were selected for the plasma etchings because of their capacity to etch oxides. Fluorocarbon plasmas produce atomic fluorine in the plasma discharge, which is responsible of the etching.<sup>49,50</sup> However, a thin fluorocarbon layer is formed during C<sub>2</sub>F<sub>6</sub> etching which limits the etching efficiency.<sup>50,51</sup> Hydrogen etching was performed after the C<sub>2</sub>F<sub>6</sub> etching due to its capacity for etching fluorocarbon film<sup>52</sup> and oxide layers<sup>45–48</sup> and to form hydroxides<sup>53,54</sup> at the oxide surface. As previously described,<sup>55</sup> the presence of hydroxides at the topmost stainless steel surface has been demonstrated to initiate the fluorocarbon film growth. Indeed, thicker coatings after 1 min deposition were observed on etched substrate in comparison with the nonetched substrate.

The aim of this work was to evaluate the influence of an interface modification by plasma etching on the stability and the corrosion protection ability of fluorocarbon films deposited on flat 316 L stainless steel substrates. Therefore, flat coated samples were deformed by a small punch test and aged in deionized water. The specimens were then thoroughly characterized by X-ray photoelectron spectroscopy (XPS), time of flight-secondary ion mass spectrometry (ToF-SIMS), ellipsometry, and atomic force microscope (AFM). Tafel measurements were used to assess the corrosion rates of the coated specimens. The characterizations were compared to those obtained from nonetched specimens.

## 2. MATERIALS AND METHODS

**2.1. Materials and Sample Preparation.** Disks of 12.7 mm diameter were punched from 316 L stainless steel plates of 0.5 mm thickness (Goodfellow, Devon, PA, USA). Flat disks were preferred to cylindrical substrates because their planar configuration allowed faster standard surface analyses (XPS, ToF-SIMS, ellipsometry and AFM). Indeed, internal studies (data not shown) of cylindrical samples showed that XPS acquisitions could last up to tens of hours. The substrates were

cleaned in an ultrasonic bath and subjected to an electropolishing and an acid dipping procedure described in detail elsewhere.<sup>56</sup> The radio frequency plasma reactor (13.56 MHz) was previously cleaned for 10 min with an oxygen plasma. Two distinct plasma etching sequences were performed on the electropolished SS316L samples prior to the coating deposition. The first plasma sequence consisted of a H<sub>2</sub> plasma and the other of a series of C<sub>2</sub>F<sub>6</sub> plasma followed by a H<sub>2</sub> plasma repeated eight times, namely etching X8. Between the etching sequences, the reactor was pump down to a base pressure lower than 10<sup>−2</sup> Torr. Pulsed afterglow plasma polymerization for five minutes in a mixture of C<sub>2</sub>F<sub>6</sub> and 6% of H<sub>2</sub> was carried out in the same reactor as the etchings to avoid contact with air. C<sub>2</sub>F<sub>6</sub> was chosen as the main precursor due to its ability to perform etching and polymerization depending on the process parameters. The details of the plasma treatments are summarized in Table 1 and were already described in detail elsewhere.<sup>55</sup>

**2.2. Deformation Method.** Coated samples were deformed up to 25% using a small-punch test device mounted on a SATEC T20000 testing machine (Instron, Norwood, MA, USA) as previously described.<sup>39,40</sup> All the deformation experiments were done in ambient air at a displacement rate of 0.05 mm/s and a maximal load of 2200 N. The subsequent analyzes were performed on the topmost layer of the deformed samples, where the 25% deformation occurs. This deformation rate was chosen in agreement with the works of Migliavacca et al.<sup>57</sup> The deformation rate in a 316 L stainless steel stent could reach up to 25% in localized areas as calculated by finite element modeling.

**2.3. Aging Tests.** Aging tests of 2 weeks in deionized water were performed in an incubator warmed at 37 ± 2 °C. The samples were inserted in a custom-made sample holder made of high density polyethylene as previously described.<sup>58</sup> Only the coated surfaces were exposed to the deionized water. Sample holders and deionized water were previously sterilized by autoclave in order to prevent bacterial contamination.

**2.4. Corrosion Tests.** The corrosion resistance of coated samples was investigated using a 1 L three-electrode glass corrosion cell and compared to as-received and electropolished 316 L stainless steel. A graphite counter-electrode was used as the auxiliary electrode and a saturated calomel electrode as the reference electrode. Measurements were performed with Model K47 Corrosion Cell System and Versa-STAT 3 Potentiostat controlled by Versa-Studio software (AMETEK Princeton Applied Research, Oak Ridge, TN, USA). Corrosion measurements were done in aerated pH 7.4 Phosphate Buffered Saline (PBS, Sigma Aldrich Canada Ltd., Oakville, On, Canada) heated at 37 ± 1 °C and stirred by mechanical agitation. The geometric area exposed to the solution was kept constant for each condition and used to determine the corrosion current density, as proposed in the ASTM G102.<sup>59</sup> Tafel extrapolation was used to calculate the corrosion rate of the samples. First, the open circuit potential (OCP) was monitored and stabilized for 1 h after the samples immersion. Then, the potential was held constant at 300 mV below the OCP for 10 min. Finally, the Tafel plot was scanned by ranging the potential between −300 mV and +1 V from OCP at a scan rate of 10 mV/s. The calculation of the corrosion rate

**Table 2.** Chemical Surface Composition of Etched and Electropolished SS316L Measured by ARXPS

sample	angle (deg)	atomic composition (%)						
		C	O	F	Cr	Fe	Ni	P
nonetched SS316L	20	44.1	40.4	1.7	4.9	5.9	0.2	2.8
	50	24.1	48.0	2.4	11.4	10.9	1.5	1.8
	90	20.1	48.2	1.5	13.8	13.2	1.9	1.4
etched H <sub>2</sub> SS316L	20	45.8	30.7	13.0	4.6	4.0	0.5	1.3
	50	19.0	31.3	25.0	11.7	10.0	2.6	0.4
	90	14.8	30.9	21.9	12.9	15.4	4.1	0.1
etched X8 SS316L	20	39.8	13.5	31.7	3.9	9.2	2.0	0
	50	15.5	9.9	50.2	6.8	15.2	2.4	0
	90	12.0	9.1	52.3	8.2	14.3	4.1	0

(CR) in mm/year is based on Faraday's law (eq 1)

$$CR = 0.003272 i_{\text{corr}} \frac{EW}{d} \quad (1)$$

where 0.003272 is a conversion factor (mm/ $\mu\text{A cm year}$ ),<sup>59</sup>  $i_{\text{corr}}$  is the corrosion current density in  $\mu\text{A/cm}^2$ ,  $EW$  is the equivalent weight of SS316L, and  $d$  is the SS316L density: 25.5 g and 8.0 g/cm<sup>3</sup>, respectively.

**2.5. Coating Characterization.** The surface composition was investigated using an X-ray Photoelectron Spectrometer (XPS - PHI 5600-ci spectrometer, Physical Electronics USA, Chanhassen, MN, USA). Survey and high-resolution spectra were acquired at a detection angle of 45° using the K $\alpha$  line of a standard aluminum and magnesium X-ray source, respectively, operated at 300 W. The curve fittings for the survey and high-resolution C(1s) peaks were determined by means of least-squares using a Shirley background subtraction. Three different spots per sample were analyzed. Angle Resolved X-ray Photoelectron Spectroscopy (ARXPS) was performed on noncoated electropolished and plasma etched SS316L using the K $\alpha$  line of a standard aluminum source operated at 300 W. ARXPS was obtained by collecting spectra from 3 takeoff angles, namely 20, 50, and 90°, which are defined as the angle between the surface and the detector.

Time of flight-secondary ion mass spectrometry (ToF-SIMS) characterizations were performed using a ToF-SIMS IV instrument (Ion-TOF GmbH, Germany) with 25 keV pulsed Ga<sup>+</sup> beam at an angle of 45° and a 1.6 pA pulsed current. Positive and negative ion mass spectra were acquired from a 50 × 50  $\mu\text{m}^2$  area. Sputtering for depth profiling was performed over a surface of 300 × 300  $\mu\text{m}^2$  with a Xe<sup>+</sup> beam of 500 eV and a current of 20 nA.

The film thickness of nondeformed samples was evaluated by ellipsometry before and after the aging tests. The measurements were done with a spectroscopic ellipsometer UVISSEL (HORIBA Yvon Jobin, Edison, NJ, USA) using 100 wavelengths from 400 to 800 nm at an incidence angle of 55°. The fluorocarbon film was fitted with the three-parameter Cauchy law. Surface imaging was performed using an atomic force microscope (AFM, Dimension 3100, Veeco, Woodbury, NY, USA) operated in tapping mode and equipped with an ultra sharp silicon tip (typical tip radius of 2 nm). Visualization and analysis of the morphology were performed using the WSxM software.<sup>60</sup>

### 3. RESULTS AND DISCUSSION

**3.1. Chemical Composition.** The surface composition of the etched SS316L was evaluated by ARXPS as shown in Table 2. XPS analyses performed at an incidence angle of 20° exhibited higher oxygen and carbon concentrations (Table 2) due to the reoxidation and organic contamination during the sample

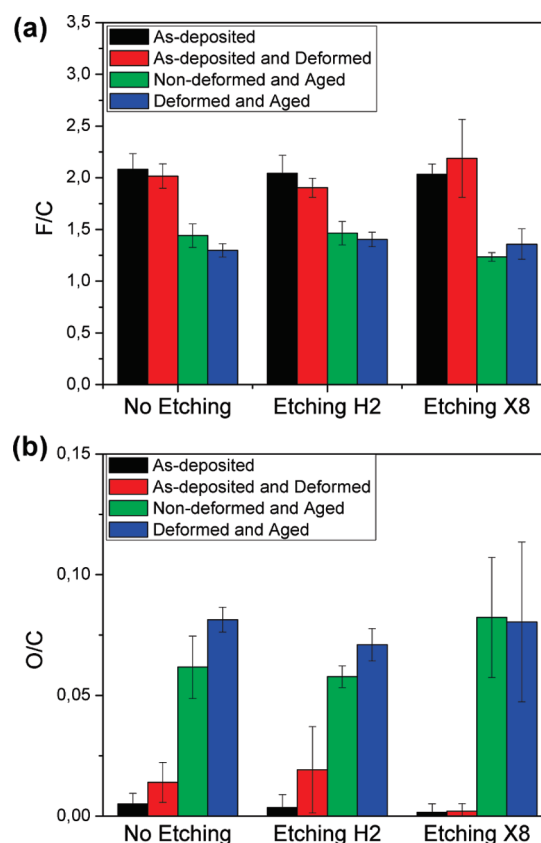


**Figure 1.** XPS (a) F/C and (b) O/C atomic ratio of as-deposited, aged, nondeformed, and deformed samples.

transfer in ambient air to the XPS chamber ( $\sim 2$  min). To lower the influence of reoxidation and organic contamination on the XPS measurements, we made the focus on the data collected at 50 and 90°. The surface of the electropolished SS316L was mainly composed of a mixture of chromium and iron oxides<sup>61–63</sup> with phosphorus contaminants due to the electropolishing process as previously observed.<sup>56</sup> The etched H<sub>2</sub> SS316L showed lower oxygen, phosphorus contents and fluorine was detected due to the contamination from the reactor wall during the hydrogen etching. The etched X8 SS316L exhibited a low oxygen and chromium concentration when compared with the other samples, which agreed with previous XPS depth profiles<sup>55</sup> and suggested the occurrence of a thinner oxide layer than etched H<sub>2</sub> and electropolished SS316L. A large amount of fluorine was detected because of its diffusion during the C<sub>2</sub>F<sub>6</sub> etchings. No phosphorus was detected on the etched X8 SS316L samples.

Thereafter, the influence of these different interfaces on the film surface composition was assessed from the XPS surveys as shown in Figure 1. After 5 min of deposition, the film chemical composition characterized by O/C and F/C ratios was not influenced by the initial interface conditions. In addition, no significant variation of the ratios was observed after the deformation, meaning that the etching procedures do not appear to influence the film cohesion. The influence of the interface on the film stability was evaluated by aging process in aqueous medium. The aged samples showed oxidation and a decrease of fluorine content, as illustrated in Figure 1, with a decrease of the fluorine–carbon ratio and an increase of the oxygen–carbon



ratio. It can be noted that the loss of fluorine and oxidation were more important for the nondeformed and aged samples etched X8. The instability of fluorocarbon films in aqueous medium could be explained by the formation of low-molecular-weight oxidized chains on the coating surface during the plasma deposition, as already described by Tanikella et al.<sup>64</sup> and Touzin et al.<sup>58</sup> Indeed, these chains are easily breakable and, upon aging, leave the surface and consequently, the fluorine concentration decreased. Similar observations were made after deformation followed by aging: oxidation and loss of fluorine were also observed with the three etching conditions.

The influence of plasma etching on the chemical composition of the film has been further investigated with high-resolution XPS, before and after deformation as well as before and after aging (Table 3). The high-resolution C(1s) spectra were decomposed in five peaks, assigned to C–H and C–C (BE = 285–285.8 eV), –C–CF (BE = 286.5–287.8 eV), –CF (BE = 288.6–290 eV), –CF<sub>2</sub> (BE = 292 eV), and –CF<sub>3</sub> (BE = 294–294.8 eV).<sup>65</sup> Typical C1s spectra before and after

aging are shown in Figure 2. As oxygen was detected in the survey spectra of the aged samples, the bands at 286.4–287 eV, 288–288.4 eV, and 289.1–289.6 eV could be also attributed to O groups such as C–O, C=O, and O–C=O, respectively.<sup>66</sup> The components of interest are C–C/C–H, CF<sub>2</sub>, and CF<sub>3</sub>, as they are directly related to chain reorganization and degradation. Indeed, CF<sub>2</sub> are characteristic of chain length, CF<sub>3</sub> of chain termination and C–C/C–H of chain breaking, reticulation, and defluorination.

The aged samples exhibited a decrease in the CF<sub>2</sub> and CF<sub>3</sub> content and the occurrence of C–C/C–H bonds, compared to the as-deposited samples, indicating a modification of the film chemistry, which agrees with the atomic ratios (Figure 1) and the formation of low-molecular-weight oxidized chains. These variations were more important for the nondeformed and aged samples etched X8, suggesting an important correlation between the film stability and the oxide layer interface. Therefore, this interface has been thoroughly investigated by ToF-SIMS with Cr<sup>+</sup> and O<sup>−</sup> depth profiles as shown in Figure 3.

**Table 3.** Component Proportions of Fluorocarbon Film Deposition on the As-Deposited and Aged Samples Measured by XPS

		proportion (%)			
		as-deposited samples		aged samples	
	component	nondeformed	deformed	nondeformed	deformed
no etching	C–C/C–H	0	0	14 ± 5	24 ± 5
	C–CF	15 ± 4	9 ± 2	16 ± 2	14 ± 3
	CF	14 ± 2	12 ± 1	13 ± 2	9 ± 1
	CF <sub>2</sub>	56 ± 7	59 ± 1	48 ± 2	43 ± 4
	CF <sub>3</sub>	16 ± 1	20 ± 2	10 ± 2	10 ± 1
etching H <sub>2</sub>	C–C/C–H	0	0	16 ± 2	19 ± 3
	C–CF	15 ± 4	17 ± 2	13 ± 3	15 ± 3
	CF	14 ± 3	17 ± 1	12 ± 4	12 ± 1
	CF <sub>2</sub>	57 ± 6	50 ± 3	48 ± 5	43 ± 1
	CF <sub>3</sub>	15 ± 1	16 ± 2	11 ± 2	10 ± 1
etching X8	C–C/C–H	0	0	23 ± 4	20 ± 6
	C–CF	15 ± 3	12 ± 3	16 ± 2	15 ± 2
	CF	13 ± 2	12 ± 3	12 ± 2	13 ± 1
	CF <sub>2</sub>	56 ± 3	59 ± 5	41 ± 1	42 ± 4
	CF <sub>3</sub>	16 ± 2	17 ± 1	9 ± 1	11 ± 2

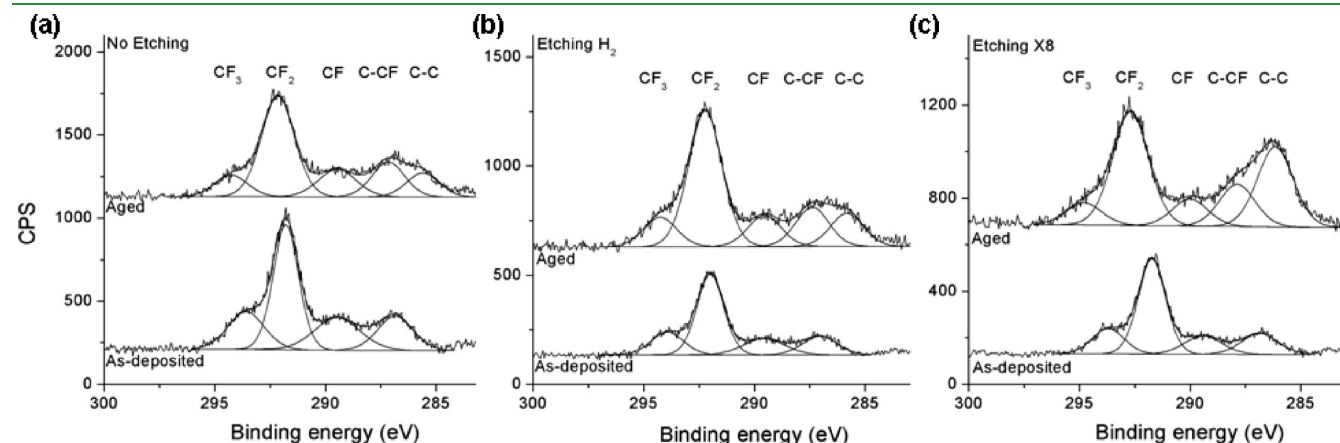


**Figure 2.** XPS high-resolution spectra of the C1(s) region of as-deposited and aged CF<sub>x</sub> films for the (a) no etching, (b) etching H<sub>2</sub>, and (c) etching X8 interface treatment.

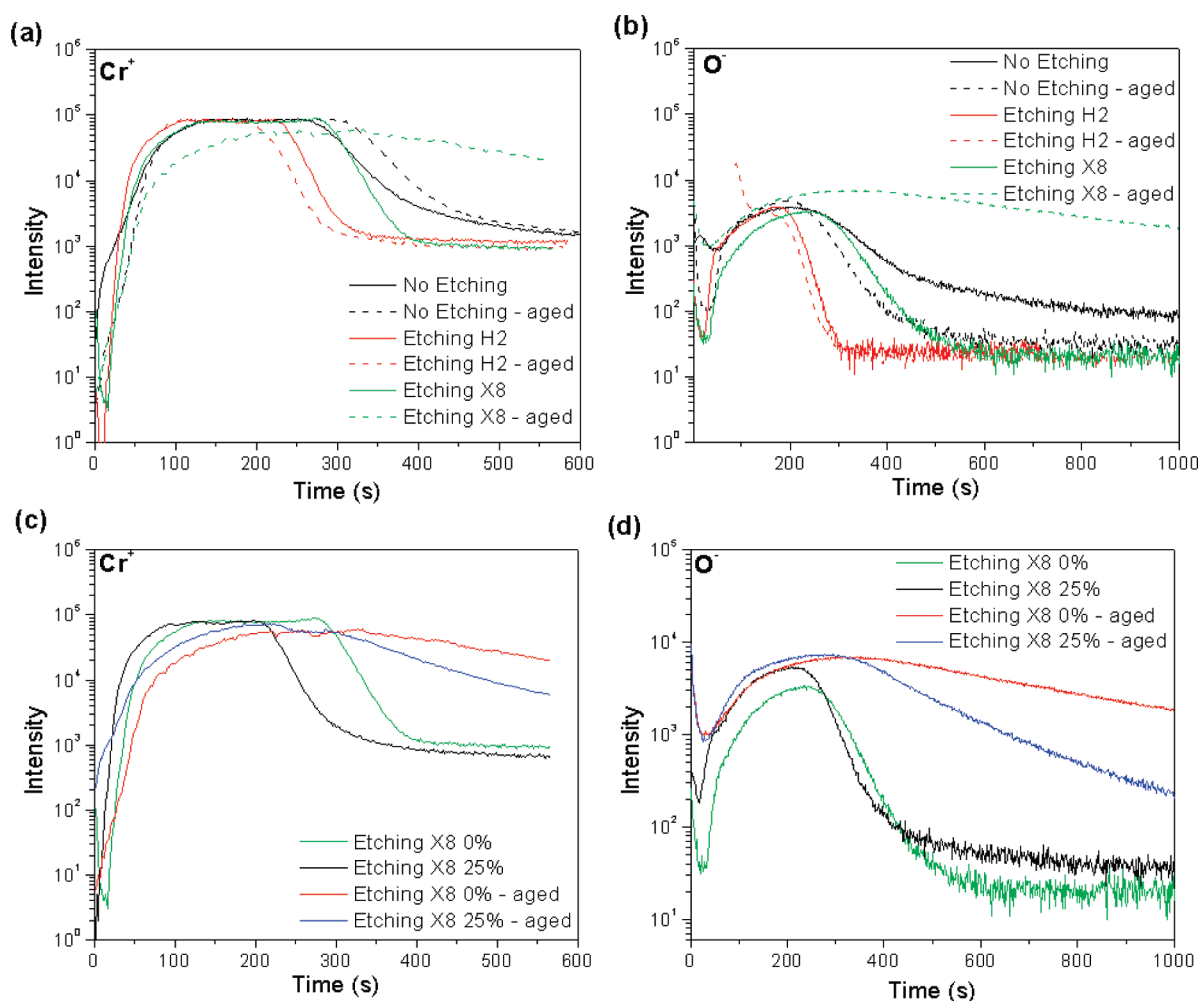


**Figure 3.** ToF-SIMS depth profile of  $\text{Cr}^+$  and  $\text{O}^-$  fragments of (a, b) as-deposited samples before and after aging and (c, d) etched X8 samples.

SS316L exhibited a layer rich in chromium and oxygen on its surface. Indeed, the formation of the  $\text{Cr}_2\text{O}_3$  layer at the stainless steel surface prevents further oxidation of the material.<sup>61</sup> One effect of the etching is the thinning of this oxide layer, as previously observed by ARXPS (Table 2). Indeed, for the nonaged samples, the  $\text{H}_2$  etching process induced a reduction of about 30% of the  $\text{Cr}^+$  and  $\text{O}^-$  plateau width compared to the nonetched sample (Figure 3a,b), which confirmed the decrease in the oxide layer thickness. However, the etched X8 and nonetched sample exhibited similar  $\text{Cr}^+$  and  $\text{O}^-$  profiles. Because ToF-SIMS analyses have been performed several days after the deposition of the film, this suggests that the etched X8 interface is prone to postoxidation. Besides, as seen in Figure 3a and 3b by the enlargement of the  $\text{Cr}^+$  and  $\text{O}^-$  fragments, the aging process provoked a significant thickening of the oxide layer on the etched X8 sample. This reoxidation is due to the X8 etching treatment, which considerably thins the oxide layer, as already reported by ARXPS (Table 2). Therefore, the etching induced a highly sensitive interface and water infiltration through nanopinhole in the coating led to a more important reoxidation. Nanopinhole have been evidenced by previous NEXAFS analyses.<sup>42</sup> Moreover, Wambach et al.<sup>67</sup> showed that the oxidation rate of the stainless steel was about 10 times higher in water than in air, which could explain the fact that the oxide layer enlargement caused by aging exceeds the thickness of the native oxide layer. It should be

**Table 4.** Film Thickness and Refractive Index before and after Aging Evaluated by Ellipsometry

	film thickness (nm)		refractive index	
	as-deposited films	aged films	as-deposited films	aged films
no etching	26 ± 11	29 ± 12	1.27 ± 0.07	1.31 ± 0.02
etching $\text{H}_2$	30 ± 2	34 ± 3	1.31 ± 0.01	1.34 ± 0.04
etching X8	34 ± 1	49 ± 2	1.31 ± 0.01	1.44 ± 0.07

noticed that the spike in the  $\text{O}^-$  profile for the aged and etched  $\text{H}_2$  sample is probably due to surface contamination. Therefore, the first few seconds of this profile were not considered in the analysis. However, as could be expected, the etched  $\text{H}_2$  interface was less sensitive, compared to the etched X8 sample, and no reoxidation occurred during aging. In agreement with these observations, the thinning and the damages caused by the plasma etchings appeared to affect the stability of the oxide layer, especially for the etched X8 samples.

Therefore, more analyses were performed on the etched X8 sample, because its interface was the most susceptible to post-oxidation. As seen in Figure 3c,d, no significant variation was observed on the oxide layer thickness after deformation (green and black curves). However, the aging induced a different

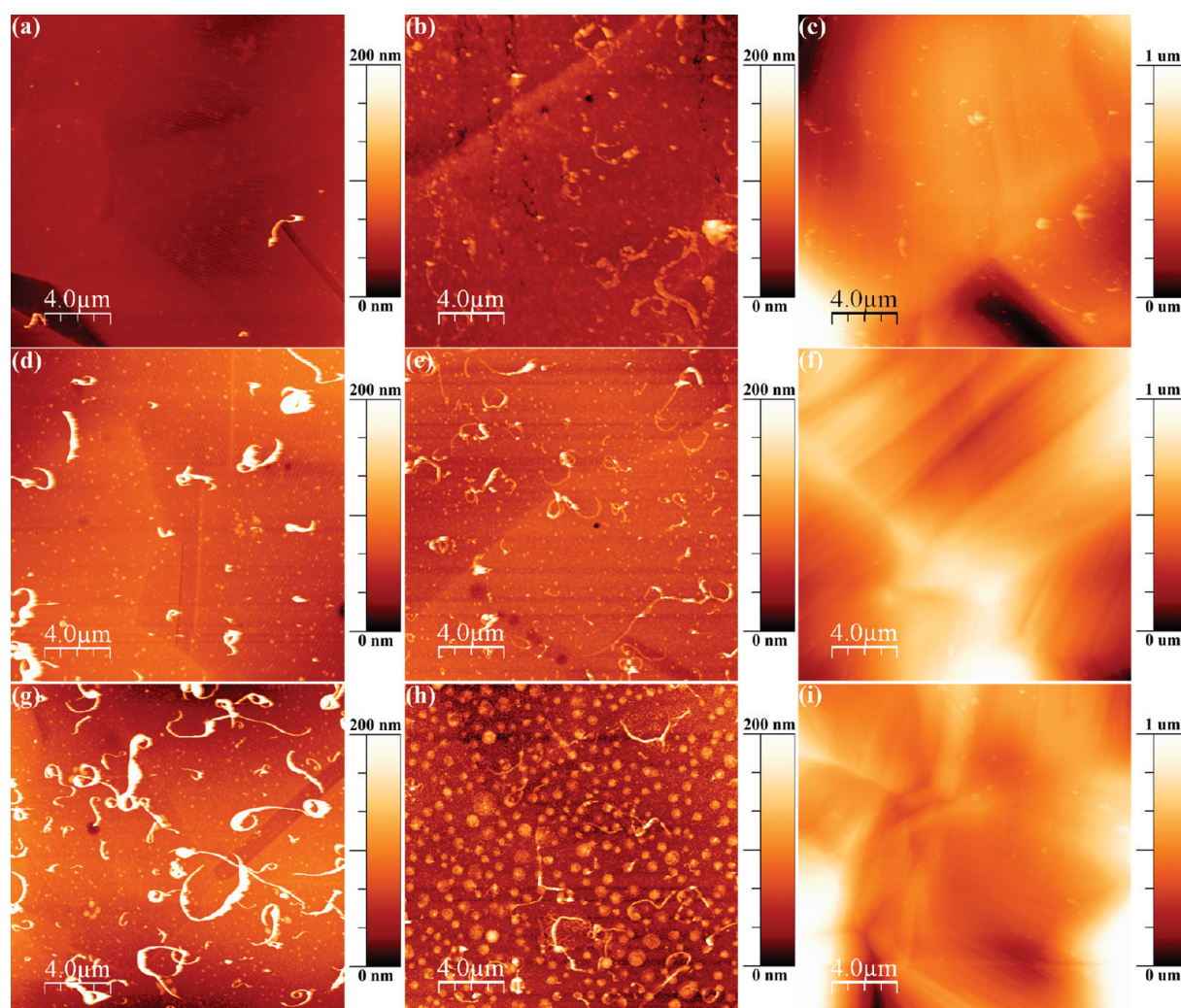


**Figure 4.** AFM images of the coated SS316L for the nonetched samples (a) as-deposited, (b) aged, (c) deformed and aged; the etching H<sub>2</sub> samples (d) as-deposited, (e) aged, (f) deformed and aged; and the etching X8 samples (g) as-deposited, (h) aged, (i) deformed and aged.

reoxidation process between the deformed and nondeformed samples (blue and red curves). This difference could be explained by the deformation of nanopinholes due to relative movements of the different layers of polymer, leading to less water infiltration.<sup>41</sup> Hence, the interface of deformed samples was probably less exposed to water and consequently displayed less reoxidation than the nondeformed and aged samples.

**3.2. Film Thickness and Morphology.** Previous results have displayed that plasma etching of the interface can affect both the initial growth of films and the stability of the interface. To assess these influences, we evaluated the film thickness by ellipsometry on three nondeformed specimens per etching treatment before and after the aging tests as summarized in Table 4. The film thickness of deformed samples was not evaluated due to the sample bending. An average thickness of about 30 nm and an index of refraction of about 1.3 were observed for the as-deposited films. Previous works on the influence of the etching treatments on the film polymerization indicated a higher growth rate during the first polymerization steps for etched X8 samples.<sup>55</sup> These differences resulted in a variation of thickness of a few nanometers after 5 min of plasma deposition. However, the nonetched samples showed an important thickness variation between the samples indicating a lack of reproducibility.

Contaminants could affect the surface chemistry of the stainless steel and the subsequent film growth. Indeed, phosphorus remained on the stainless steel after the electropolishing as observed by ARXPS in Table 2.

After the aging tests, only the etched X8 specimens displayed a significant change of the film thickness (around +40%) and refractive index (around +10%). The refractive index of the fluorocarbon films calculated at a wavelength of 800 nm is shown in Table 4. The thickness and chemical composition variations due to aging could be partly provoked by water intake as previously observed by Touzin et al.<sup>58</sup> Chemical modifications of the interface and the film are also capable of influencing the film thickness measurement. However, ToF-SIMS characterizations (Figure 3) suggested that increases in thickness and refractive index could be explained by the postoxidation of the oxide layer due to the aging. In this context, higher variations, as observed in Table 4, were expected from the etched X8 samples since its oxide-depleted interface has a greater sensitivity to reoxidation through nanopinholes. Because the substrate used in the ellipsometry model was an electropolished SS316L sample for all etching conditions, the variation of the oxide layer thickness caused by the different etching pretreatments was not directly considered. Besides, the refractive indexes at a



**Table 5. Corrosion Rates of Nondeformed and Deformed Samples**

samples	corrosion rates ( $\mu\text{m}/\text{year}$ )	
	nondeformed	deformed
as-received SS316L	$4.1 \pm 0.1$	$5.88 \pm 0.06$
electropolished SS316L	$1.0 \pm 0.3$	$3.6 \pm 0.5$
coated electropolished SS316L	$0.41 \pm 0.01$	$0.7 \pm 0.3$
coated $\text{H}_2$ etched SS316L	$1.1 \pm 0.4$	$1.7 \pm 0.3$
coated X8 etched SS316L	$11 \pm 2$	$2.3 \pm 0.2$

wavelength of 800 nm of the  $\text{Cr}_2\text{O}_3$  and  $\text{Fe}_2\text{O}_3$  are about  $2.3^{68,69}$  and  $2.7^{69}$  respectively, which are higher than the one of the fluorocarbon film ( $\sim 1.3$ ). This suggests that the thickness and the refractive index measured on the etched samples are then an average of one of the fluorocarbon film and the oxide layer. Therefore, it seems reasonable to suggest that the increases observed by ellipsometry on the aged samples etched X8 are due to the creation of a thicker, postoxidized interfacial oxide layer formed during aging, as confirmed by ToF-SIMS.

To understand the effects of etchings on surface features and the coating stability, the film morphology was visualized by AFM as shown in Figure 4. As-deposited films exhibited, in Figure 4a, d, g, a similar surface with the formation of a uniform film over the SS316L surface with the growth of ribbonlike features. These features are formed during the film polymerization due to the migration of adsorbed radicals during the off time of the pulsed plasma discharge as explained by Millela et al.<sup>70</sup> The increasing size and number of ribbons can be explained by the presence of hydroxide bonds at the substrate surface and their importance in the initiation of polymerization. Thus, the etched X8 sample in Figure 3g showed the highest amount of ribbons due to a higher concentration of hydroxides at the interface, as previously reported,<sup>55</sup> and is therefore in a more advanced state of polymerization. Ribbons reached heights up to 400 nm on the etched X8 samples.

After the aging tests, circular protrusions, resulting from water infiltration through nanopinholes<sup>55</sup> as mentioned previously, were observed in Figure 4 b, e, h on the nondeformed samples. The size and the height of the protrusions were higher for the etched X8 samples. In agreement with the ToF-SIMS depth profiles, these protrusions could be due to localized subcoating oxidation hence swelling of the interfacial region. After the 25% deformation and the two weeks immersion in deionized water, the morphology of the samples is dominated by the movement of substrate grains and the occurrence of slip bands as observed in Figure 4c, f, i. No coating delamination or cracks were observed on all samples even after an aging of two weeks, indicating that the coating adhesion and cohesion is sufficient to resist to a stent expansion, since the deformation method replicates the maximum expansion of a stent.<sup>57</sup> Protrusions were observable on the aged and deformed etched X8 samples, but with a lower density as compared to the nondeformed etched X8 samples. As no major modification of the film chemistry between the nondeformed and deformed aged samples was observed by XPS (Figure 1), the decrease in the occurrence of protrusions could be explained by the deformation of the nanopinholes.<sup>41</sup> Also, ToF-SIMS profiles (Figure 3d) showed less oxidation of the interface for the deformed sample due to the aging compared to the nondeformed sample.

**3.3. Corrosion Rates.** Corrosion rates calculated from the Tafel plots were used to quantify the influence of interface modifications on the barrier properties of plasma fluorocarbon films. Corrosion rates of nondeformed and deformed samples are shown in Table 5. Electropolished SS316L showed a higher corrosion resistance as compared to the as-received SS316L due to the uniformity of the new oxide layer formed after the electropolishing.<sup>71–73</sup> Fluorocarbon films deposited on the electropolished SS316L lowered the corrosion rate by about a factor of 2, which indicates a better corrosion protection provided by the fluorocarbon films. Coated and etched samples exhibited a higher corrosion rates as compared to the coated and electropolished samples. It is important to note that the influence of the surface roughness on the corrosion rate is negligible in our case, since AFM measurements showed that coated and electropolished samples have similar roughness of about 7–9 nm over a surface area of  $20 \times 20 \mu\text{m}^2$ .<sup>55</sup> Also, the difference between the real and geometric area due to surface roughness was inferior to 5% for as-received and deformed samples. The importance of the chromium oxide layer thickness and its enrichment in Cr(VI) for the corrosion protection of stainless steel was demonstrated in the works of Wallinder et al.<sup>74</sup> and Shahryari et al.<sup>75</sup> Plasma etchings performed in this work decreased the oxide layer thickness and chromium content as previously observed<sup>55</sup> and therefore decreased the corrosion protection of the coated samples. Also, NEXAFS measurements performed at selected linearly polarized light, revealed an increased linearity of the polymeric structure for the etched X8 and coated samples, indicating straighter nanopores which would therefore make the coating more permeable/conductive even if the pores are less numerous. That corroborates the AFM observations of less dense but larger protrusions due to interfacial corrosion for these samples. Corrosion tests of etched surfaces before coating would have been interesting to further investigate the effects of roughness and thickness of the oxide layer on the corrosion rate but were not reported due to fast reoxidation of the specimen when exiting the reactor.

After the 25% deformation, the corrosion rates for most of the samples increased except for the etched X8 samples. However, the film provided a corrosion resistance with the decrease in the corrosion rate by about a factor of 5 when comparing the noncoated with the coated electropolished SS316L. The increase of the film barrier properties may be explained by the vertical movement and the fragmentation of the nanopinholes as suggested by Hale et al.<sup>41</sup> The deformed and etched X8 samples showed a different trend with the decrease of the corrosion rate. This different behavior could be attributed to less numerous but straighter nanopores that, once deformed, become individually no more permeable/conductive than the deformed nanopores of the coatings on the otherwise prepared substrates. Collectively, they therefore become less permeable/conductive.

## 4. CONCLUSION

This work investigated the effects of plasma etchings prior to plasma polymerization on the film stability and corrosion resistance properties. Plasma etchings, by modifying the chromium oxide layer of stainless steel, were essential in order to obtain reproducible coatings, to initiate the polymerization and to lower the nanopore density. Thereby, no delamination and cracking were detected on the deformed and aged samples for both studied etchings, indicating that they are an efficient way to promote adhesion and cohesion of the fluorocarbon film.



On the other hand, the aging test results suggested that the oxide layer thinning produced by plasma etchings seemed to affect both the film and the interface stability. Protrusions were observed by AFM and their density and size were higher on the nondeformed and etched samples, especially for the etched X8 samples. Their occurrence could be due to localized oxidation of the interfacial region of the stainless steel due to water diffusion through nanopinholes. Moreover, etched X8 samples also showed the highest variations in ToF-SIMS, XPS and ellipsometry results after two weeks aging, showing that thinner oxide layers are more unstable and prone to postoxidation.

Plasma fluorocarbon films were effective to protect the stainless steel from corrosion. The corrosion rates were decreased by a factor of 2 before the deformation and by a factor of 5 after the 25% deformation. However, the plasma etchings provoked the oxide layer thinning, which could not be compensated, in terms of corrosion, by the coating deposition, hence the decrease in the barrier properties. Further work should investigate methods to stabilize the interface without degrading the film coverage and to lower the nanopores connectivity.

## AUTHOR INFORMATION

### Corresponding Author

\*E-mail: Diego.Mantovani@gmn.ulaval.ca. Address: Laboratory for Biomaterials and Bioengineering, Department of Materials Engineering, Pavillon Adrien-Pouliot, 1745-E Laval University, Quebec City, Canada QC, G1K 7P4. Phone: (418) 656-2131 ext. 6270. Fax: (418) 656-5343. URL: www.lbb.gmn.ulaval.ca.

## ACKNOWLEDGMENT

The authors thank Marie Leroy for her help in the corrosion experiments. The authors are grateful to Bastian Douhard of the Laboratoire Interdisciplinaire de Spectroscopie Electronique in Namur (Belgium) for his help and advices in the ToF-SIMS experiments. The help and guidance of Dr. Servaas Holvoet and Dr. Paula Horny are also deeply acknowledged. This work was partially supported by the Natural Sciences and Engineering Research Council of Canada and by the University Hospital Research Center (St. François d'Assise Hospital) in Quebec City.

## REFERENCES

- Morita, S.; Tamano, J.; Hattori, S.; Ieda, M. *J. Appl. Phys.* **1980**, *51*, 754–758.
- Shofield, W. C. E.; Badyal, J. P. S. *ACS Appl. Mater. Interfaces* **2009**, *1*, 2763–2767.
- Arefi-Khonsari, F.; Tatoulian, M.; Brétagne, F.; Bouloussa, O.; Rondelez, F. *Surf. Coat. Technol.* **2005**, *200*, 14–20.
- Tatoulian, M.; Brétagne, F.; Arefi-Khonsari, F.; Amouroux, J.; Bouloussa, O.; Rondelez, F.; Paul, A. J.; Mitchell, R. *Plasma Process. Polym.* **2005**, *2*, 38–44.
- Kobayashi, H.; Bell, A. T.; Shen, M. *Macromolecules* **1974**, *3*, 277–283.
- Wertheimer, M. R.; Klemberg-sapieha, J. E.; Schreiber, H. P. *Thin Solid Films* **1984**, *115*, 109–124.
- Inagaki, N.; Kondo, S.; Hirata, M.; Urushibata, H. *J. Appl. Polym. Sci.* **1985**, *30*, 3385–3395.
- Liu, D.; Cuddy, M. F.; Fisher, E. R. *ACS Appl. Mater. Interfaces* **2009**, *1*, 934–943.
- Iwamori, S.; Tanabe, T.; Yano, S.; Noda, K. *Surf. Coat. Technol.* **2010**, *204*, 2803–2807.
- Matsumoto, Y.; Ishida, M. *Sens. Actuators, A* **2000**, *83*, 179–185.
- Shi, F. F. *Surf. Coat. Technol.* **1996**, *82*, 1–15.
- Arefi-Khonsari, F.; Kurdi, J.; Tatoulian, M.; Amouroux, J. *Surf. Coat. Technol.* **2001**, *142–144*, 437–448.
- Yasuda, H. *J. Membr. Sci.* **1984**, *18*, 273–284.
- Yasuda, H.; Gazicki, M. *Biomaterials* **1982**, *3*, 68–77.
- Delattre, J. L.; d'Agostino, R.; Fracassi, F. *Appl. Surf. Sci.* **2006**, *252*, 3912–3919.
- López-Santos, C.; Yubero, F.; Cotrino, J.; González-Elipse, A. R. *ACS Appl. Mater. Interfaces* **2010**, *2*, 980–990.
- Bierwagen, G. P.; He, L.; Ellingson, L.; Tallman, D. E. *Prog. Org. Coat.* **2000**, *39*, 67–78.
- Burt, H. M.; Hunter, W. L. *Adv. Drug Delivery Rev.* **2006**, *58*, 350–357.
- Shaulov, Y.; Okner, R.; Levi, Y.; Tal, N.; Gutkin, V.; Mandler, D.; Domb, A. J. *ACS Appl. Mater. Interfaces* **2009**, *1*, 2519–2528.
- O'Brien, B.; Carroll, W. *Acta Biomater.* **2009**, *5*, 945–958.
- Eisenberg, M. J.; Konnyu, K. *J. Am. J. Cardiol.* **2006**, *98*, 375–382.
- Tatoulian, M.; Gallino, E.; Jafari, R.; Arefi-Khonsari, F.; Tatoulian, L.; Borra, J. P.; Lewis, F.; Mantovani, D. *Mater. Sci. Forum* **2007**, *539–543*, 529–534.
- Park, J.; Shin, D.; Kim, Y. *J. Invasive Cardiol.* **2007**, *19*, E43–E45.
- Cosgrave, J.; Melzi, G.; Corbett, S.; Biondi-Zoccai, G. G. L.; Babic, R.; Airolidi, F.; Chieffo, A.; Sangiorgi, G. M.; Montorfano, M.; Michev, I.; Carlino, M.; Colombo, A. *Am. Heart J.* **2007**, *153*, 354–359.
- Woods, T. C.; Marks, A. R. *Annu. Rev. Med.* **2004**, *55*, 169–178.
- Regar, E.; Sianos, G.; Serruys, P. W. *Br. Med. Bull.* **2001**, *59*, 227–248.
- Lahann, J.; Klee, D.; Thelen, H.; Bienert, H.; Vorwerk, D.; Hoecker, H. *J. Mater. Sci.—Mater. Med.* **1999**, *10*, 443–448.
- Hanefeld, P.; Westedt, U.; Wombacher, R.; Kissel, T.; Schaper, A.; Wendorff, J.; Greiner, A. *Biomacromolecules* **2006**, *7*, 2086–2090.
- Unger, F.; Westedt, U.; Hanefeld, P.; Wombacher, R.; Zimmermann, S.; Greiner, A.; Ausborn, M.; Kissel, T. *J. Controlled Release* **2007**, *117*, 312–321.
- Otsuka, Y.; Chronos, N.; Apkarian, R.; Robinson, K. *J. Invasive Cardiol.* **2007**, *19*, 71–76.
- Wiemer, M.; Butz, T.; Schmidt, W.; Schmitz, K. P.; Horstkotte, D.; Langer, C. *Catheter. Cardiovasc. Interv.* **2010**, *75*, 905–911.
- Seal, B. L.; Otero, T. C.; Panitch, A. *Mater. Sci. Eng., R* **2001**, *34*, 147–230.
- Pruitt, L. A. In *Encyclopedia of Materials: Science and Technology*; Buschow, K. H. J., Ed.; Elsevier Science: Oxford, U.K., 2008; p 3216.
- Ramakrishna, S.; Mayer, J.; Wintermantel, E.; Leong, K. W. *Compos. Sci. Technol.* **2001**, *61*, 1189–1224.
- Chevallier, P.; Janvier, R.; Mantovani, D.; Laroche, G. *Macromol. Biosci.* **2005**, *5*, 829–839.
- Favia, P.; d'Agostino, R. *Surf. Coat. Technol.* **1998**, *98*, 1102–1106.
- Xue, L.; Greisler, H. P. *J. Vasc. Surg.* **2003**, *37*, 472–480.
- Lewis, F.; Horny, P.; Hale, P.; Turgeon, S.; Tatoulian, M.; Mantovani, D. *J. Phys. D: Appl. Phys.* **2008**, *41*, 045310.
- Lewis, F.; Mantovani, D. *Macromol. Mater. Eng.* **2009**, *294*, 11–19.
- Lewis, F.; Maheux-Lacroix, B.; Turgeon, S.; Mantovani, D. In *Adhesion Aspects of Thin Films*; Mittal, K. L., Ed.; V.S.P. Intl Science: Leiden, The Netherlands, 2007; Vol. 3, p 71.
- Hale, P.; Turgeon, S.; Horny, P.; Lewis, F.; Brack, N.; Van Riessen, G.; Pigram, P.; Mantovani, D. *Langmuir* **2008**, *24*, 7897–7905.
- Chevallier, P.; Holvoet, S.; Turgeon, S.; Horny, P.; Pireaux, J. J.; Mantovani, D. *J. App. Polym. Sci.* **2011**, *118*, 3176–3186.
- d'Agostino, R.; Cramarossa, F.; Colaprico, V.; d'Ettola, R. *J. Appl. Phys.* **1983**, *54*, 1284–1288.
- d'Agostino, R.; Cramarossa, F.; Illuzzi, F. *J. Appl. Phys.* **1987**, *61*, 2754–2762.
- Bertrand, N.; Bulkin, P.; Drévilion, B.; Lucas, S.; Benayoun, S. *Surf. Coat. Technol.* **1997**, *94–95*, 362–367.
- Mozetic, M. *Vacuum* **2001**, *61*, 367–371.
- Mozetic, M.; Zalar, A.; Drobnic, M. *Thin Solid Films* **1999**, *343–344*, 101–104.

- (48) Figueroa, C. A.; Alvarez, F. *Appl. Surf. Sci.* **2006**, *253*, 1806–1809.
- (49) d'Agostino, R.; Capezzuto, P.; Bruno, G.; Cramarossa, F. *Pure Appl. Chem.* **1985**, *57*, 1287–1298.
- (50) Gaboriau, F.; Fernandez-Peignon, M. C.; Cartry, G.; Cardinaud, C. *J. Vac. Sci. Technol., A* **2005**, *23*, 226–233.
- (51) Butoi, C. I.; Mackie, N. M.; Williams, K. L.; Capps, N. E.; Fisher, E. R. *J. Vac. Sci. Technol., A* **2000**, *18*, 2685–2698.
- (52) Seo, H.; Kim, S. B.; Song, J.; Kim, Y.; Soh, H.; Kim, Y. C.; Jeon, H. *J. Vac. Sci. Technol., B* **2002**, *20*, 1548–1555.
- (53) Li, Y. S.; Wong, P. C.; Mitchell, K. A. R. *Appl. Surf. Sci.* **1995**, *89*, 263–269.
- (54) Sawada, Y.; Tamaru, H.; Kogoma, M.; Kawase, M.; Hashimoto, K. *J. Phys. D: Appl. Phys.* **1996**, *29*, 2539–2544.
- (55) Lewis, F.; Turgeon, S.; Chevallier, P.; Pireaux, J. J.; Tatoulian, M.; Mantovani, D. *Plasma Process. Polym.* **2010**, *7*, 309–317.
- (56) Haidopoulos, M.; Turgeon, S.; Sarra-Bournet, C.; Laroche, G.; Mantovani, D. *J. Mater. Sci.—Mater. Med.* **2006**, *17*, 647–657.
- (57) Migliavacca, F.; Petrini, L.; Montanari, V.; Quagliana, I.; Auricchio, F.; Dubini, G. *Med. Eng. Phys.* **2005**, *27*, 13–18.
- (58) Touzin, M.; Chevallier, P.; Lewis, F.; Turgeon, S.; Holvoet, S.; Laroche, G.; Mantovani, D. *Surf. Coat. Technol.* **2008**, *202*, 4884–4891.
- (59) ASTM G102–89, *Standard Practice for Calculation of Corrosion Rates and Related Information from Electrochemical Measurements*; ASTM International: West Conshohocken, PA, 1994.
- (60) Horcas, I.; Fernández, R.; Gómez-Rodríguez, J. M.; Colchero, J. G.-H., J.; Baro, A. M. *Rev. Sci. Instrum.* **2007**, *78*, 013705.
- (61) Adams, R. O. *J. Vac. Sci. Technol., A* **1983**, *1*, 12–18.
- (62) Mantel, M.; Wightman, J. P. *Surf. Interface Anal.* **1994**, *21*, 595–605.
- (63) Olsson, C. O. A.; Landolt, D. *Electrochim. Acta* **2003**, *48*, 1093–1104.
- (64) Tanikella, R.; Agraharam, S.; Bidstrup Allen, S.; Hess, D.; Kohl, P. *J. Electron. Mater.* **2002**, *31*, 1096–1103.
- (65) Favia, P. In *Plasma Polymer Films*; Biederman, H., Ed.; Imperial College Press: London, 2004; p 25.
- (66) Silverstein, M. S.; Sandrin, L.; Sacher, E. *Polymer* **2001**, *42*, 4299–4307.
- (67) Wambach, J.; Wokaun, A.; Hiltzold, A. *Surf. Interface Anal.* **2002**, *34*, 164–170.
- (68) Al-Kuhaili, M. F.; Durrani, S. M. A. *Opt. Mater.* **2007**, *29*, 709–713.
- (69) Karlsson, B.; Ribbing, C. G. *J. Appl. Phys.* **1982**, *53*, 6340–6346.
- (70) Milella, A.; Palumbo, F.; Favia, P.; Cicala, G.; d'Agostino, R. *Pure Appl. Chem.* **2005**, *77*, 399–414.
- (71) Beddoes, J.; Bucci, K. J. *J. Mater. Sci.—Mater. Med.* **1999**, *10*, 389–394.
- (72) Jenkinson, D. *Corros. Mater.* **2002**, *27*, 10–13.
- (73) Lee, S.-J.; Lai, J.-J. *J. Mater. Process. Technol.* **2003**, *140*, 206–210.
- (74) Wallinder, D.; Pan, J.; Leygraf, C.; Delblanc-Bauer, A. *Corros. Sci.* **1998**, *41*, 275–289.
- (75) Shahryari, A.; Omanovic, S.; Szpunar, J. A. *J. Biomed. Mater. Res., Part A* **2009**, *89A*, 1049–1062.